

Research Article

A Blast-Resistant Method Based on Wave Converters with Spring Oscillator for Underground Structures

Yu Zhang,¹ Yuanxue Liu,¹ Runze Wu,¹ Jichang Zhao,¹ Ming Hu,¹ and Yizhong Tan²

¹Chongqing Key Laboratory of Geomechanics & Geoenvironmental Protection, Logistical Engineering University, Chongqing, China

²PLA Engineering College, Xuzhou, China

Correspondence should be addressed to Yuanxue Liu; 357202780@qq.com

Received 20 January 2017; Accepted 12 April 2017; Published 10 May 2017

Academic Editor: Nuno M. Maia

Copyright © 2017 Yu Zhang et al. This is an open access article distributed under the Creative Commons Attribution License, which permits unrestricted use, distribution, and reproduction in any medium, provided the original work is properly cited.

Researches on blast-resistant measures for underground structures such as tunnels and underground shopping malls are of great importance for their significant role in economic and social development. In this paper, a new blast-resistant method based on wave converters with spring oscillator for underground structures was put forward, so as to convert the shock wave with high frequency and high peak pressure to the periodic stress wave with low frequency and low peak pressure. The conception and calculation process of this new method were introduced. The mechanical characteristics and motion evolution law of wave converters were deduced theoretically. Based on the theoretical deduction results and finite difference software FLAC^{3D}, the dynamic responses of the new blast-resistant structure and the traditional one were both calculated. Results showed that, after the deployment of wave converters, the peak absolute values of the bending moment, shear force, and axial force of the structure decreased generally, which verified the good blast-resistant effect of the new blast-resistant method.

1. Introduction

Tunnels, subway stations, underground shopping malls, and so forth play an important role in the economic and social development, as well as the personal and property safety. In recent years, there have been a variety of researches on the blast-resistant measures for underground structures, mainly focused on the design and optimization on structures and materials.

Blast-resistant measures based on the structure optimization mainly contain the increase of stiffness or adoption of structures good for the reflection, diffraction, and scattering of the stress wave. Usually the arch structures and structures containing holes have better performance of wave dissipation than rectangular structures or structures without holes, so these kinds of structures have attracted many attentions of scholars [1–3]. A good blast-resistant performance is also embodied in the plate-foam composite structure [4], box-shaped steel plate-reinforced concrete composite structure [5], carbon fiber reinforced composite structure [6, 7], and prestressed structure [8]. Via the explosion model tests, Yang et al. studied the antiexplosion effect of prestressed

cable reinforced caverns. The results showed that prestressed structures are good for antiexplosion [9]. Kobiela et al. experimentally investigated the influence of an attenuation barrier on soil stresses and pressures acting on a buried silo, caused by underground explosions at different distances. Test results verified the blast-resistant effectiveness caused by the barrier composed of the cylindrical tubes [10]. The dynamic response of a buried silo caused by underground explosion was also studied experimentally via the measured pressures [11].

Blast-resistant measures based on the material optimization are mainly concentrated on the development of porous or lightweight materials of low stiffness, and the materials are developing gradually from the traditional inorganic porous materials or lightweight materials to the polymer materials and porous metal materials currently. Materials such as the rigid polyurethane foam, polypropylene fiber concrete, rubber concrete, foam concrete, foamed aluminium, and steel fiber reinforced concrete are good choices for the blast-resistant materials. Yakushin et al. investigated the properties of low-density rigid polyurethane foams with hollow glass

microspheres. The tension and compression properties in relation to the content of microspheres were determined in their work [12]. Alhozaimy et al. found that the flexural toughness and impact resistance showed an increase in the presence of polypropylene fibers [13]. The mechanical properties of concrete containing tire-rubber particles were studied by Khaloo et al. [14]. They found that, unlike plain concrete, the failure state in rubberized concrete occurred gently and uniformly and did not cause any separation in the specimen. In fact, this property is good for dynamic protection. Hernández-Olivares and Barluenga also studied the fire performance of the rubber-filled concrete [15]. Lim et al. studied the compressive, splitting tensile, and flexural strengths of lightweight foamed concrete [16]. The results have shown that the foamed concrete is a good choice for dynamic protection.

In the blast-resistant methods of the traditional structure optimization, the construction process is usually complex, and sometimes the function of structures may even be affected. The shock wave mainly consists of high frequency components. In the blast-resistant methods of porous or lightweight materials, the materials are easy to get damaged unrecoverably and have large deformation under the blasting load because of the low elastic modulus and the existence of the holes. Thereby the overall stability of underground structure and surrounding rock may be affected by the large deformation.

In order to improve the traditional antiknock methods, a new blast-resistant method based on wave converters with spring oscillator for underground structures is put forward in this paper. The new method mainly consists of an array of wave converters and a distribution layer. Firstly, the conception of the new method is introduced, including the formation of the wave converter and distribution layer. Secondly, the calculation process of dynamic responses for underground structures adopting the new blast-resistant method is presented. Thirdly, the mechanical characteristics and motion evolution law of the wave converter are derived, including the static constitutive relation of the wave converter, dynamic response partitioning of the wave converter, differential equation of motion for the spring oscillator, displacement transfer coefficient of the wave converter, and the stress inversion of the wave converter. A case study is also conducted to verify the applicability and rationality of the new method by comparing with the traditional structure.

2. Conception of New Blast-Resistant Method

The new method mainly consists of an array of wave converters and a distribution layer, shown in Figure 1. The wave converter includes 2 shells containing a length adjusting rod and a spring oscillator comprised of springs and a mass block, shown in Figure 2. The initial length of the wave converter can be adjusted via the adjustment of the length adjusting rod, which can control the prestress of the compression springs. Via the adjustment of the initial converter length, the wave converter can also be easily installed under different reserve space between the rock and tunnel roof. The wave converter is compressible when the load on the top of

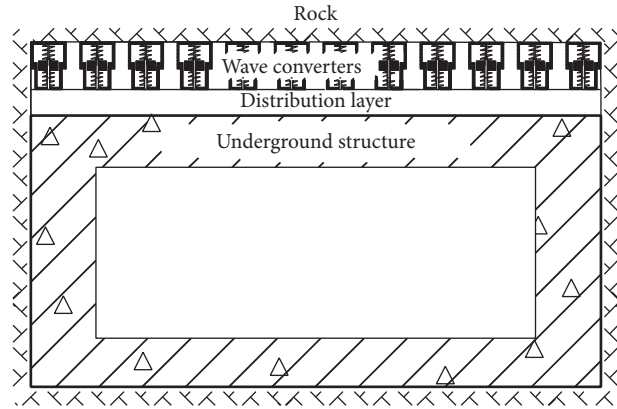


FIGURE 1: Schematic of the new blast-resistant method.

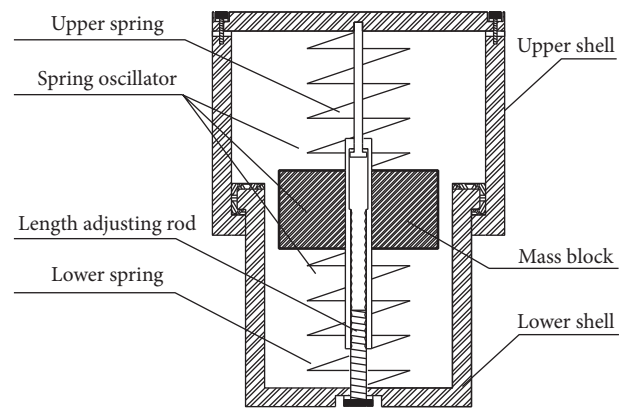


FIGURE 2: Schematic of the wave converter.

the converter exceeds the spring prestress. The distribution layer is composed of the material with relatively low wave impedance, shown in Figure 1. Multiple reflections caused by the periodic stress wave can occur in the distribution layer, which results in the further energy dissipation.

The new blast-resistant method combines such mechanisms as the spring deformation, inertia, and periodic vibration of the mass block to provide the resistance against the dynamic load. The self-support capacity of the surrounding rock can also be fully utilized. Via the wave converter, the shock wave with high frequency and high peak pressure can be transformed to the periodic stress wave with low frequency and low peak pressure. Thereby the shock wave is dispersed and materials under the converter can be prevented from crushing. Under the blasting load, the deformation process of the wave converter can be divided into such 3 periods as rapid loading stage, rapid unloading stage, and slow unloading stage.

The above 3 stages are determined by the relative displacement $\Delta u_i(t)$ between the top and bottom of wave converter. Under the impact loads propagating in the rock, the typical curve of $\Delta u_i(t)$ with time for the wave converter is shown in Figure 3. As is shown in Figure 3, the rapid loading stage corresponds to the sharp increasing period, and the rapid unloading stage corresponds to the fast decreasing period,

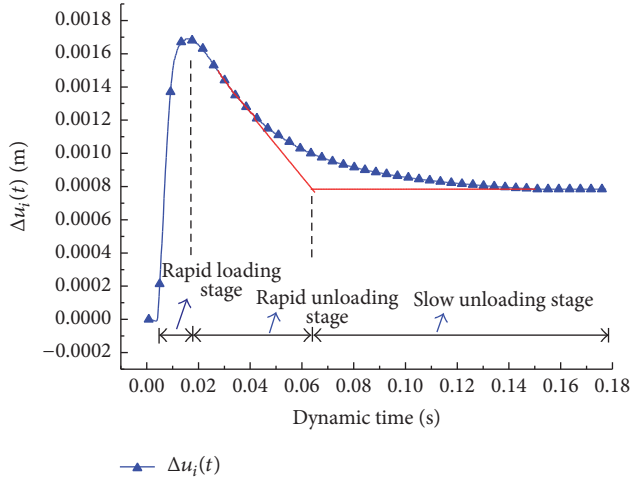


FIGURE 3: Typical curve of $\Delta u_i(t)$ with time for the wave converter.

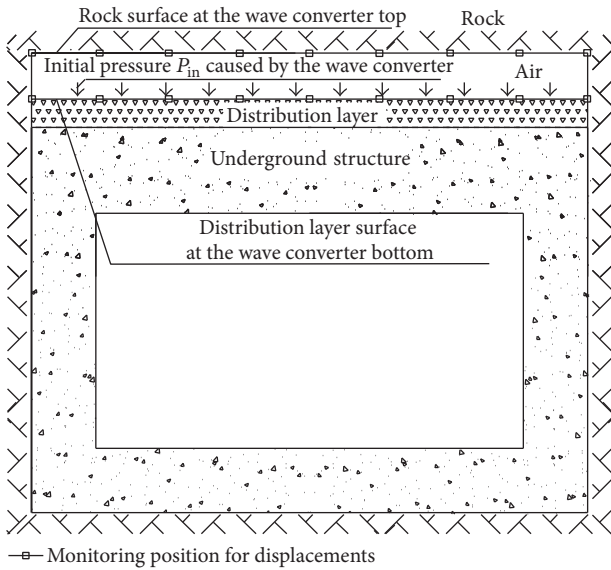


FIGURE 4: Schematic of model 1.

while the slow unloading stage corresponds to the slow change period.

3. Calculation Process of Dynamic Responses for Structures with the New Blast-Resistant Method

(1) Establish numerical models and acquire the data needed for the calculation of the wave converter's displacements in the rapid loading stage and rapid unloading stage. Model 1 without wave converters for the finite element analysis is set up, shown in Figure 4. In model 1, the distribution layer, underground structure, and rock are established. The initial pressure caused by the wave converter on the distribution layer surface (at the wave converter bottom) is applied as the lower spring force divided by the cross-sectional

area of the wave converter. Then the explosion position and blasting load should be applied. After that, under the blasting load, the finite element analysis method is used to calculate the vertical displacement-time curves $u_{0i}(t)$ and $u_{2i}(t)$ of the rock surface at the wave converter top and the distribution layer surface at the wave converter bottom, respectively. The monitoring positions for displacements are suggested to adopt the tops and bottoms of 9 wave converters along the width direction of the structure, shown in Figure 4. Then model 2 of the ground without any construction such as the structure, distribution layer, and wave converters is built up, shown in Figure 5. The numerical analysis based on model 2 under the same explosion condition as model 1 is conducted to obtain the vertical rock pressure-time curve $P_{A0}(t)$ for the corresponding monitoring positions of the rock surface in model 1, shown in Figure 5.

- (2) Solve the differential equation of motion for the spring oscillator and obtain the law of motion in the rapid loading stage and rapid unloading stage. In model 1, the vertical displacement-time curve $u_{0i}(t)$ of the rock surface at the wave converter top multiplied by a displacement transfer coefficient K_i ($0 < K_i < 1$) is considered as the vertical displacement-time curve $u_{1i}(t)$ of the wave converter top in the rapid loading stage and rapid unloading stage of the true situation. The true situation refers to the real underground structure with an array of wave converters and a distribution layer. The vertical displacement-time curve $u_{2i}(t)$ of the distribution layer surface at the wave converter bottom in model 1 is considered directly as the vertical displacement-time curve of the wave converter bottom in the rapid loading stage and rapid unloading stage of the true situation. In the true situation, the difference between $u_{1i}(t)$ and $u_{2i}(t)$ is the relative displacement $\Delta u_i(t)$ between the top and bottom of the wave converter. The wave converter is in the rapid loading stage before the relative displacement reaches the maximum, while it is in the rapid unloading stage during the sharp decrease period after the relative displacement reaches the maximum. Taking the displacements of the wave converter top and bottom as the boundary condition, the differential equation of motion for the spring oscillator can be solved to obtain the law of motion in the rapid loading stage and rapid unloading stage. Then the stress-time curve of the wave converter top and bottom in above 2 stages can be gotten.
- (3) Solve the differential equation of motion for the spring oscillator and obtain the law of motion in the slow unloading stage. According to step (2), the length of the wave converter, the displacement (or position coordinate) and velocity of the oscillator at the end of the rapid unloading step can be gotten. Then the differential equation of motion for the spring oscillator in the slow unloading stage can be solved. In the slow unloading stage, the length of the wave

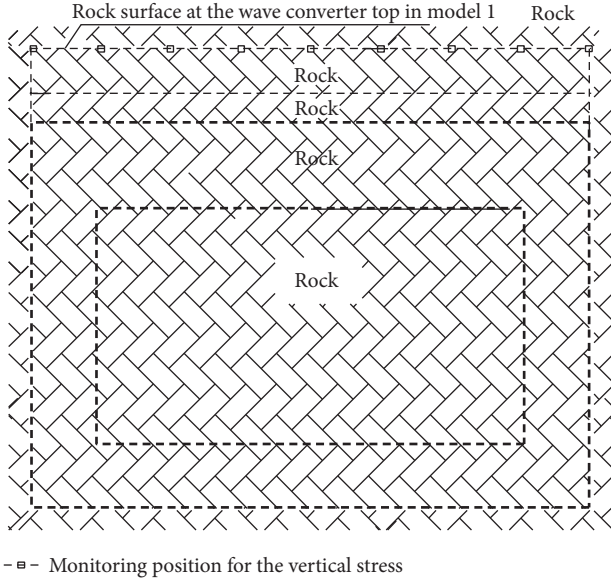


FIGURE 5: Schematic of model 2.

converter can be deemed as a constant. In that case the calculation results of the dynamic response are a little dangerous which would be safer for the structure design. After that, the stress-time curve of the wave converter top and bottom in the slow unloading stage can be gotten.

- (4) Calculate the dynamic response of the underground structure. Firstly, the initial pressure P_{in} caused by the wave converter on the distribution layer surface in model 1 should be deleted. Then the stress-time curves of the wave converter top and bottom in three stages are applied on the rock surface and distribution layer surface, instead of the wave converters. After that, the blasting load is applied and the dynamic calculation is conducted to get the dynamic response of the structure.

4. Mechanical Characteristics and Motion Evolution Law of Wave Converters

4.1. Static Constitutive Relation of the Wave Converter. l_0 is the initial length of the wave converter, while a is the shell thickness. So the initial clear length of the wave converter can be written as $l_{n0} = l_0 - 2a$, and l_{n0} is shown in Figure 6. In Figure 6, the dashed line is the position under the static equilibrium, and the solid line is the position at any time under the dynamic load. k_1 is the stiffness coefficient of the upper spring, whose length in free state is l_{10} . Δx_{10} is the initial amount of compression for upper spring. k_2 is the stiffness coefficient of the lower spring, and l_{20} is its length in free state. Δx_{20} is the initial amount of compression for lower spring. m and l_3 are the mass and height of the mass block, respectively. $P_A(t)$ is the vertical rock pressure on the wave converter top in the true situation, while $P_{A0}(t)$ is the vertical rock pressure at the same location in model 2. When the wave

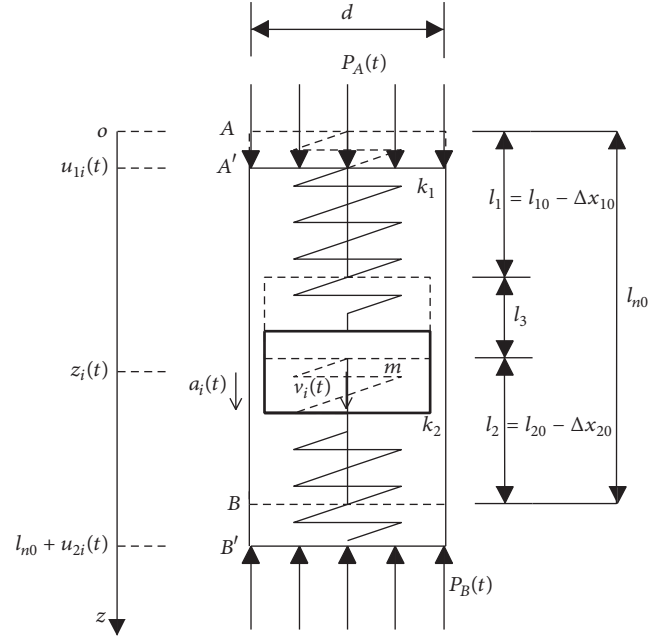


FIGURE 6: Deformation process of the wave converter.

converter is installed with the initial length l_0 , under static equilibrium, the geometric equation is established, yielding

$$l_{n0} = l_1 + l_2 + l_3 = l_{10} + l_{20} + l_3 - \Delta x_{10} - \Delta x_{20}. \quad (1)$$

As for the mass block, the balance equation is

$$mg + k_1 \Delta x_{10} = k_2 \Delta x_{20}. \quad (2)$$

Combining (1) and (2), the solutions are

$$\Delta x_{10} = \frac{k_2 (l_{10} + l_{20} + l_3 - l_{n0}) - mg}{k_1 + k_2}, \quad (3)$$

$$\Delta x_{20} = \frac{mg}{k_2} + \frac{k_1 (l_{10} + l_{20} + l_3 - l_{n0})}{k_1 + k_2} - \frac{k_1 mg}{k_2 (k_1 + k_2)}.$$

F_1 and F_2 are the force of upper and lower springs, respectively. s is the cross-sectional area of the wave converter. d is the cross-sectional length. If the weight of the wave converter's shells is ignored, F_1 can be expressed as

$$F_1(t) = \begin{cases} k_1 \Delta x_{10}, & sP_A(t) < k_1 \Delta x_{10} \\ sP_A(t), & sP_A(t) \geq k_1 \Delta x_{10}; \end{cases} \quad (4)$$

F_2 can be expressed as

$$F_2(t) = \begin{cases} mg + k_1 \Delta x_{10} & sP_A(t) < k_1 \Delta x_{10} \\ sP_A(t) + mg & sP_A(t) \geq k_1 \Delta x_{10}. \end{cases} \quad (5)$$

So the static constitutive relation of the wave converter yields

$$\text{If } sP_A(t) < k_1 \Delta x_{10}, \quad \Delta l = 0 \quad (6)$$

$$\text{If } sP_A(t) \geq k_1 \Delta x_{10}, \quad \Delta l = (k_1 + k_2) \left\{ \frac{sP_A(t)}{k_1 k_2} + \frac{[mg - k_2(l_{10} + l_{20} + l_3 - l_{n0})]}{k_2(k_1 + k_2)} \right\}. \quad (7)$$

4.2. Dynamic Response Partitioning of the Wave Converter. The rapid loading stage, rapid unloading stage, and slow unloading stage correspond to the rapid compression stage, rapid recovery stage, and slow recovery stage, respectively. In the slow recovery stage, the length of the wave converter can be deemed as a constant. The demarcation point of stage 1 and stage 2 is that the relative displacement reaches the maximum. The duration time of stage 2 can be determined by the relative displacement-time curve. When the rock masses above the structure are in a wide range of elasticity state, the rapid unloading stage can not be ignored, but if the rock masses are in a wide range of plastic state, the rapid unloading stage can be ignored.

The computing time of stage 3 is advisable for 1 or 2 vibration periods. Via a large amount of computations, it is concluded that the computing time of stage 3 can be taken as 1 vibration period if stage 2 can not be ignored; otherwise it can be taken as 2 vibration periods.

4.3. Differential Equation of Motion for the Spring Oscillator

4.3.1. Differential Equation of Motion in Rapid Loading Stage and Rapid Unloading Stage. N is the total number of wave converters along the width direction of the structure, and i is the serial number of the wave converter. For wave converter i , $u_{0i}(t)$ is the vertical displacement of the rock surface at the wave converter top in model 1, and $u_{2i}(t)$ ($i = 1, 2, \dots, n$) is the vertical displacement of the wave converter bottom in

rapid loading stage and rapid unloading stage of the true situation. $u_{1i}(t)$ is the vertical displacement of the wave converter top in rapid loading stage and rapid unloading stage of the true situation, which can be expressed as $u_{1i}(t) = K_i u_{0i}(t)$. K_i is the displacement transfer coefficient of the wave converter. $\Delta u_i(t)$ is the relative displacement between the top and bottom of the wave converter, which can be written as $\Delta u_i(t) = u_{1i}(t) - u_{2i}(t)$. At the end of the rapid unloading stage is the initial state of the slow unloading stage, which can be deemed as the fixed-length vibration, shown in Figure 7. In Figure 7, the dashed line is the position under the static equilibrium in the fixed-length vibration, and the solid line is the position at the end of the rapid unloading stage.

As is shown in Figure 6, $v_i(t)$, $a_i(t)$, and $z_i(t)$ are oscillator velocity, oscillator acceleration, and position coordinate at the time of t , respectively, yielding

$$v_i(t) = \frac{dz_i(t)}{dt}. \quad (8)$$

The length of the upper spring is

$$l_{1i}(t) = z_i(t) - u_{1i}(t) - \frac{l_3}{2}. \quad (9)$$

The amount of the spring compression is

$$\Delta x_{1i}(t) = l_{10} - z_i(t) + u_{1i}(t) + \frac{l_3}{2}. \quad (10)$$

The length of the lower spring is

$$l_{2i}(t) = l_{n0} + u_{2i}(t) - z_i(t) - \frac{l_3}{2}. \quad (11)$$

The amount of the spring compression is

$$\Delta x_{2i}(t) = l_{20} - l_{n0} - u_{2i}(t) + z_i(t) + \frac{l_3}{2}. \quad (12)$$

The oscillator acceleration yields

$$a_i(t) = \frac{k_1 \Delta x_{1i}(t) + mg - k_2 \Delta x_{2i}(t)}{m} = \frac{k_1(l_{10} - z_i(t) + u_{1i}(t) + l_3/2) + mg - k_2(l_{20} - l_{n0} - u_{2i}(t) + z_i(t) + l_3/2)}{m}. \quad (13)$$

Then the differential equation of motion for the spring oscillator is

$$\begin{aligned} & \frac{d^2 z_i(t)}{dt^2} + \frac{(k_1 + k_2)}{m} z_i(t) \\ &= \frac{k_1}{m} u_{1i}(t) + \frac{k_2}{m} u_{2i}(t) \\ & \quad - \frac{k_2(l_{20} - l_{n0}) - mg - k_1 l_{10} - (k_1 - k_2) l_3/2}{m}. \end{aligned} \quad (14)$$

The above equation is an ordinary differential equation of the second order, which can be solved by the Runge-Kutta method of the fourth order. This equation can be transformed to following forms:

$$\begin{aligned} & z_i''(t) = f(t, z_i(t), z_i'(t)), \quad t_0 \leq t \leq t_n \\ & z_i(t_0) = l_1 + \frac{l_3}{2}, \\ & z_i'(t_0) = 0. \end{aligned} \quad (15)$$

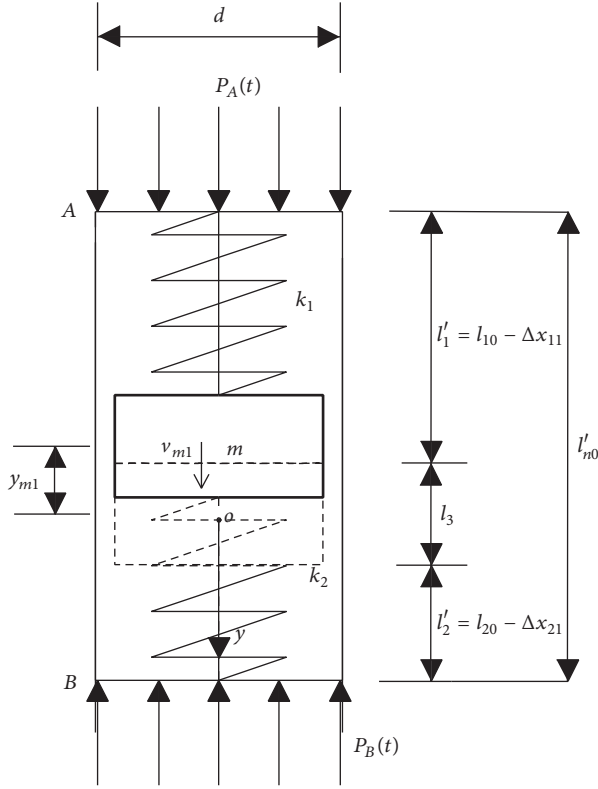


FIGURE 7: Initial state of the fixed-length vibration.

Assuming that $w_i(t) = z'_i(t)$, the above equations can be written as following ordinary differential equations of the first order

$$\begin{aligned}
 z'_i(t) &= w_i(t), \\
 z_i(t_0) &= l_1 + \frac{l_3}{2}, \\
 w'_i(t) &= f(t, z_i(t), w_i(t)) \\
 &= \frac{k_1}{m} u_{1i}(t) + \frac{k_2}{m} u_{2i}(t) \\
 &\quad - \frac{k_2(l_{20} - l_{n0}) - mg - k_1 l_{10} - (k_1 - k_2) l_3 / 2}{m} \\
 &\quad - \frac{(k_1 + k_2)}{m} z_i(t).
 \end{aligned} \tag{16}$$

According to the Runge-Kutta method of the fourth order [17, 18], its numerical calculation formula can be represented as

$$\begin{aligned}
 z_{i(j+1)}(t_0 + (j+1)h) \\
 &= z_{ij}(t_0 + jh) + \frac{h}{6} (K_1 + 2K_2 + 2K_3 + K_4), \\
 w_{i(j+1)}(t_0 + (j+1)h) \\
 &= w_{ij}(t_0 + jh) + \frac{h}{6} (M_1 + 2M_2 + 2M_3 + M_4),
 \end{aligned} \tag{17}$$

where

$$\begin{aligned}
 K_1 &= w_{ij}(t_0 + jh), \\
 M_1 &= \frac{k_1}{m} u_{1i}(t_0 + jh) + \frac{k_2}{m} u_{2i}(t_0 + jh) \\
 &\quad - \frac{k_2(l_{20} - l_0) - mg - k_1 l_{10}}{m} \\
 &\quad - \frac{(k_1 + k_2)}{m} z_{ij}(t_0 + jh), \\
 K_2 &= w_{ij}(t_0 + jh) + \frac{h}{2} M_1, \\
 M_2 &= \frac{k_1}{m} u_{1i}\left(t_0 + jh + \frac{h}{2}\right) + \frac{k_2}{m} u_{2i}\left(t_0 + jh + \frac{h}{2}\right) \\
 &\quad - \frac{k_2(l_{20} - l_0) - mg - k_1 l_{10}}{m} \\
 &\quad - \frac{(k_1 + k_2)}{m} \left[z_{ij}(t_0 + jh) + \frac{h}{2} K_1 \right], \\
 K_3 &= w_{ij}(t_0 + jh) + \frac{h}{2} M_2, \\
 M_3 &= \frac{k_1}{m} u_{1i}\left(t_0 + jh + \frac{h}{2}\right) + \frac{k_2}{m} u_{2i}\left(t_0 + jh + \frac{h}{2}\right) \\
 &\quad - \frac{k_2(l_{20} - l_0) - mg - k_1 l_{10}}{m} \\
 &\quad - \frac{(k_1 + k_2)}{m} \left[z_{ij}(t_0 + jh) + \frac{h}{2} K_2 \right], \\
 K_4 &= w_{ij}(t_0 + jh) + h M_3, \\
 M_4 &= \frac{k_1}{m} u_{1i}(t_0 + (j+1)h) + \frac{k_2}{m} u_{2i}(t_0 + (j+1)h) \\
 &\quad - \frac{k_2(l_{20} - l_0) - mg - k_1 l_{10}}{m} \\
 &\quad - \frac{(k_1 + k_2)}{m} [z_{ij}(t_0 + jh) + h K_3].
 \end{aligned} \tag{18}$$

Given the displacement boundary conditions of the wave converter top and bottom ($u_{1i}(t)$, $u_{2i}(t)$), the position coordinate $z_i(t)$ and velocity $v_i(t)$ of the oscillator at the time of t can be derived. Therefore, the amount of the compression $\Delta x_{1i}(t)$, $\Delta x_{2i}(t)$ can be obtained.

4.3.2. Differential Equation of Motion in Slow Unloading Stage.

In the slow unloading stage, the vertical displacements of the wave converter top and bottom have few changes over time, so the length of the wave converter can be considered as a constant. l'_0 and l'_{n0} are the length and clear length of the wave converter at the end of the rapid unloading stage, respectively. As is shown in Figure 7, the geometry of the wave converter at the end of the rapid unloading stage is drawn in the solid line, while the dashed line shows the static

equilibrium position of the mass block. The y -axis is vertical downward and its coordinate origin is the static equilibrium position of the mass block in stage 3. In Figure 7, at the end of the rapid unloading stage, v_{m1} is the oscillator velocity, and y_{m1} is the distance from the oscillator center to that of the static equilibrium position.

If the oscillator is in static equilibrium under the converter length of l'_0, l'_{n0} yields

$$l'_{n0} = l_{10} + l_{20} + l_3 - \Delta x_{11} - \Delta x_{21}. \quad (19)$$

The balance equation for the mass block is

$$mg + k_1 \Delta x_{11} = k_2 \Delta x_{21}, \quad (20)$$

where Δx_{11} and Δx_{21} are the amount of compression for upper and lower spring in static equilibrium under the converter length of l'_0 , respectively. Δx_{11} and Δx_{21} are

$$\begin{aligned} \Delta x_{11} &= \frac{k_2 (l_{10} + l_{20} + l_3 - l'_{n0}) - mg}{k_1 + k_2}, \\ \Delta x_{21} &= \frac{mg}{k_2} + \frac{k_1 (l_{10} + l_{20} + l_3 - l'_{n0})}{k_1 + k_2} - \frac{k_1 mg}{k_2 (k_1 + k_2)}, \end{aligned} \quad (21)$$

F_i, f_{Ii} , and S_i are the active force, inertia force, and constraint counterforce, respectively. Based on the D'Alembert principle, F_i, f_{Ii} , and S_i yield

$$F_i + S_i + f_{Ii} = 0. \quad (22)$$

The active force consists of the gravity force mg , damping force f_D , and elastic restoring force f_s . Then (22) can be written as

$$m\ddot{y}_m(t) + c\dot{y}_m(t) + (k_1 + k_2)y_m(t) = 0. \quad (23)$$

$y_m(t)$ is the position coordinate of the oscillator in y coordinate. The time at the end of the rapid unloading stage is assumed as t_u , and then the position coordinate and velocity of the oscillator can be expressed as $z_i(t_u)$ and $v_i(t_u)$ in z coordinate. Via the coordinate transform, the position coordinate and velocity of the oscillator in y coordinate can be expressed as y_{m1} and v_{m1} . y_{m1} and v_{m1} are the initial conditions of (23), so the solution of (23) is

$$y_m(t) = A \cos \omega_D t + B \sin \omega_D t, \quad (24)$$

where

$$\begin{aligned} A &= y_{m1} e^{-\zeta \omega_n t}, \\ B &= \frac{v_{m1} + \zeta \omega_n y_{m1}}{\omega_D} e^{-\zeta \omega_n t}, \\ \omega_D &= \omega_n \sqrt{1 - \zeta^2}, \\ \omega_n &= \sqrt{\frac{k_1 + k_2}{m}}; \end{aligned} \quad (25)$$

ζ is the damping ratio. If $\zeta = 0$, the calculation results of the dynamic response are a little dangerous which would be safer for the structure design, so ζ is considered as 0 in the analysis of stage 3. Considering that $y_m(t)$ is solved, the amount of compression for springs at any time can be obtained. After that, the stress-time curve of the wave converter top and bottom in the slow unloading stage can be gotten.

4.4. Displacement Transfer Coefficient of the Wave Converter.

In the rapid loading stage and rapid unloading stage, based on the numerical calculations in model 1 and model 2, the following equation can be derived:

$$\frac{sP_{A0}(t)/w}{u_{0i}(t)} = \frac{sP_{A0}(t)/w - F_1 [K_i u_{0i}(t) - u_{2i}(t)]}{K_i u_{0i}(t)}, \quad (26)$$

where w is the area ratio of the wave converter's cross-sectional area, and w is equal to all wave converters' cross-sectional areas divided by the area of rock surface above the structure. According to (4) and (7), when $sP_A(t) \geq k_1 \Delta x_{10}$, the constitutive relation for the wave converter can be modified as

$$\begin{aligned} &K_i u_{0i}(t) - u_{2i}(t) \\ &= F_1 [K_i u_{0i}(t) - u_{2i}(t)] \frac{k_1 + k_2}{k_1 k_2} \\ &\quad - \frac{(k_1 + k_2)(l_{10} + l_{20} + l_3 - l_{n0}) - mg}{k_1 + k_2} \\ &\quad + \frac{k_1 mg}{k_2 (k_1 + k_2)}. \end{aligned} \quad (27)$$

Combining (26) and (27), K_i yields

$$K_i = \frac{(k_1 + k_2) sP_{A0}(t) + wk_1 k_2 u_{2i}(t) + wk_1 [mg - k_2 (l_{10} + l_{20} + l_3 - l_{n0})]}{wk_1 k_2 u_{0i}(t) + (k_1 + k_2) sP_{A0}(t)}. \quad (28)$$

4.5. Stress Inversion of the Wave Converter. Based on the solutions on differential equations of motion in 3 stages, if the gravity force of the wave converter shell is ignored, the stress-time curves of the wave converter top and bottom in 3 stages can be gotten.

In stage 1 and stage 2, the function of the stress-time curve of the wave converter top is

$$P_{1i}(t) = \frac{k_1 \Delta x_{1i}(t)}{s} = \frac{k_1 (l_{10} - z_i(t) + u_{1i}(t) + l_3/2)}{s}. \quad (29)$$

TABLE 1: Mechanical parameters for the rock.

Density (kg/m ³)	Elastic modulus (GPa)	Poisson ratio	Cohesion (MPa)	Internal friction angle (°)	Tensile strength (MPa)
2400	13	0.28	1.1	45	0.91

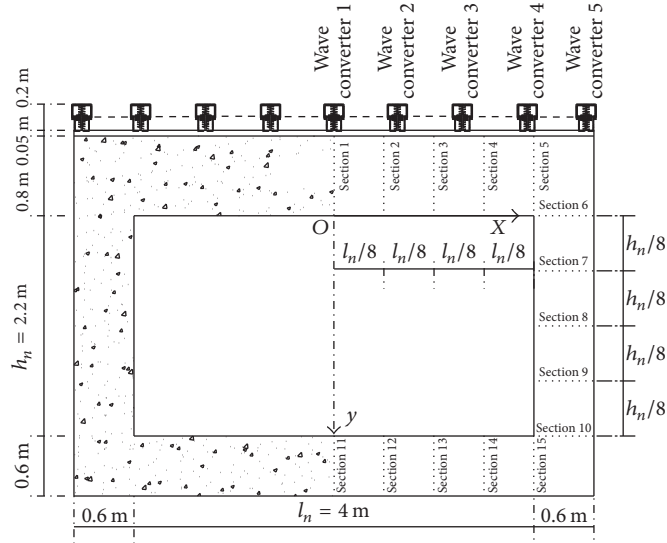


FIGURE 8: Structure size and monitoring sections for internal forces in case 1.

The function of the stress-time curve of the wave converter bottom is

$$\begin{aligned}
 P_{2i}(t) &= \frac{k_2 \Delta x_{2i}(t)}{s} \\
 &= \frac{k_2 (l_{20} - l_{n0} - u_{2i}(t) + z_i(t) + l_3/2)}{s}
 \end{aligned} \quad (30)$$

In stage 3, the functions of the stress-time curves of the wave converter top and bottom are, respectively,

$$\begin{aligned}
 P_{1i}(t) &= \frac{k_1 (\Delta x_{11} - y_m(t))}{s} \\
 &= \frac{k_1 \Delta x_{11} - k_1 (A \cos \omega_n t + B \sin \omega_n t)}{s}, \\
 P_{2i}(t) &= \frac{k_2 (\Delta x_{21} + y_m(t))}{s} \\
 &= \frac{k_2 \Delta x_{21} + k_2 (A \cos \omega_n t + B \sin \omega_n t)}{s}.
 \end{aligned} \quad (31)$$

Then, in model 1, the initial pressure P_{in} caused by the wave converter on the distribution layer surface is deleted, and the stress-time curves of the wave converter top and bottom in three stages are applied on the rock surface and distribution layer surface, respectively. After that, the blasting load is applied and the dynamic calculation is conducted to get the dynamic response of the structure (shown in calculation process (4)).

5. Case Study

5.1. Case Set-Up. Based on the software of FLAC^{3D}, 2 kinds of cases are set up to conduct the dynamic analysis. Case 1 is the traditional underground structure without the new blast-resistant method, while case 2 is the underground structure with the mentioned new blast-resistant method. Compared with case 2, the difference in case 1 is that the wave converter and distribution layer are not set.

Figure 8 shows the structure size and monitoring sections for internal forces in case 2, and the monitoring sections for internal forces are the same as case 1. The size of the structure is designed according to literature [19], and the buried depth is 10 m. Mechanical parameters for the rock and structure are listed in Tables 1 and 2. The distribution layer is made up of the foam concrete which has the density of 799 kg/m³ and thickness of 0.05 m. The mechanical parameters of the foam concrete are shown in Table 3 [20]. In case 2, the tops and bottoms of wave converters 1~5 are chosen as monitoring positions for displacements and stresses, shown in Figure 8, and the interpolation is used to get the stresses of other wave converters. The wave converter is a cubic structure with the side length of 0.2 m. $l_0 = 0.2$ m, $a = 0.05$ m, $w = 100\%$, $k_1 = k_2 = 100$ kN/m, $l_{10} = l_{20} = 0.05$ m. $l_3 = 0.14$ m, $m = 38.9$ kg.

The width, height, and thickness of the numerical models are 35.2 m, 28.85 m, and 1 m, respectively. The blasting load is assumed as a triangle wave acting on the ground surface (in Figure 9), and the loading scope is from -3 m to 3 m on x -axis. The lifting duration and drop duration of the blast pressure-time curve are set as 1 ms and 6 ms according to the literature [21], respectively. The peak of the shock wave

TABLE 2: Mechanical parameters for the structure.

Density (kg/m ³)	Elastic modulus (GPa)	Poisson ratio	Cohesion (MPa)	Internal friction angle (°)
2400	30	0.21	3.68	58.7

TABLE 3: Mechanical parameters for foam concrete.

Density (kg/m ³)	Elastic modulus (GPa)	Poisson ratio	Cohesion (MPa)	Internal friction angle (°)	Tensile strength (MPa)
799	0.342	0.1	0.17	29	0.2

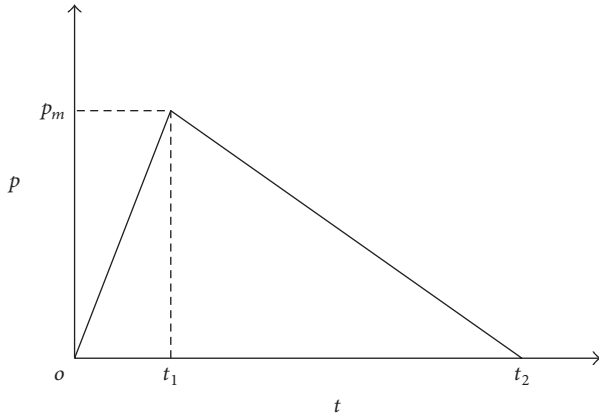
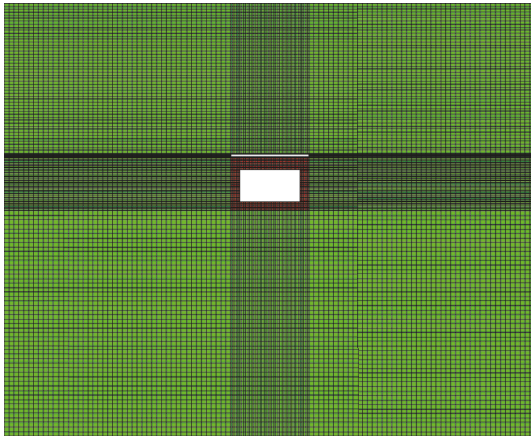


FIGURE 9: Curve of the blasting load.

FIGURE 10: Model 1 built up based on FLAC^{3D} for numerical calculation.

pressure p_m is 0.6 GPa. Model 1 built up based on FLAC^{3D} for numerical calculation is shown in Figure 10.

According to the symmetry, the monitoring positions for displacements are suggested to adopt the tops and bottoms of 5 wave converters along the width direction of the structure, shown in Figure 8. In order to obtain the internal forces such as the bending moment, axial force, and shear force of the structure, a total of 15 monitoring sections are set up, shown in Figure 8.

5.2. Analysis of the Calculation Results. The curves of the displacement transfer coefficient K_i with time in the rapid

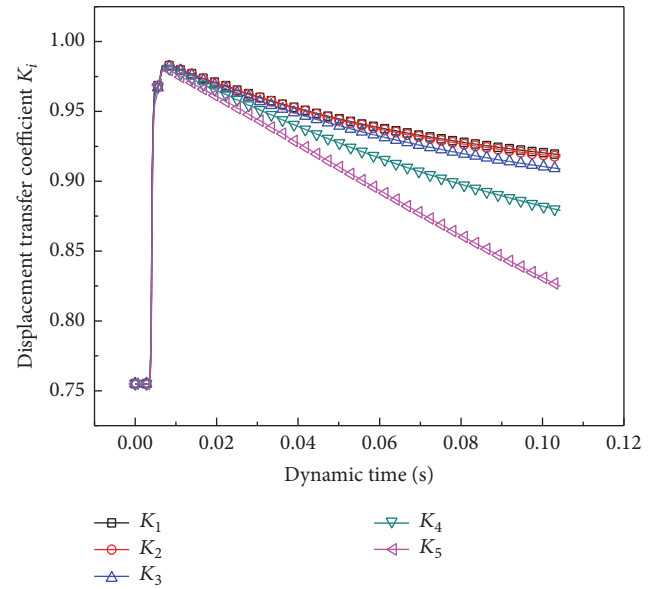


FIGURE 11: Curves of the displacement transfer coefficient with time.

loading and rapid unloading stages are shown in Figure 11, and i represents the serial number of the wave converter. The curves of $u_{0i}(t)$, $u_{1i}(t)$, $u_{2i}(t)$, and $\Delta u_i(t)$ with time are shown in Figures 12–15, respectively. In all 3 stages of the wave converter deformation, the stress-time curves of the wave converter top are shown in Figure 16, while the stress-time curves of the wave converter bottom are shown in Figure 17. The internal forces such as the bending moment, axial force, and shear force are listed in Tables 4–6.

In Tables 4–6, the bending moment resulting in the tensile stress in the inner element of the structure is positive. The positive shear force is by counterclockwise, while the axial force to tension is positive. It can be concluded that the peak absolute value of the bending moment in case 2 is generally lower than that of case 1, and the maximum drop in the roof, side wall, and floor is 57.3%, 69.7%, and 52.7%, respectively.

The peak absolute value of the shear force for monitoring sections in case 2 is also generally lower than that of case 1. The maximum drop in the roof, side wall, and floor is 86.2%, 75.6%, and 33.1%, respectively. The peak absolute value of the axial force for monitoring sections in case 2 is remarkably lower than that of case 1. The maximum drop in the roof, side wall, and floor is 44.7%, 74.7%, and 37.2%, respectively. For the roof, the decrease of the axial tensile force near the midspan is obvious, and the maximum drop occurs to the

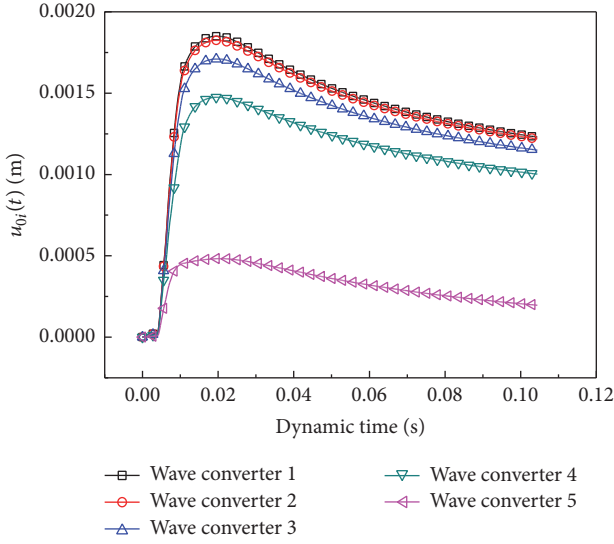


FIGURE 12: Curves of $u_{0i}(t)$ with time.

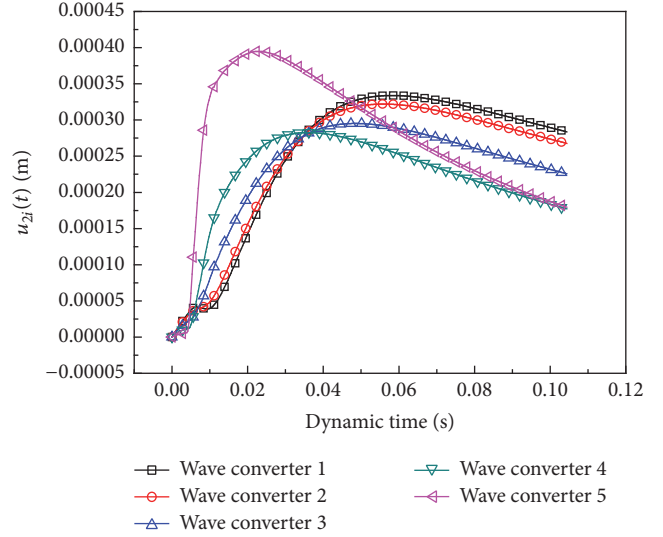


FIGURE 14: Curves of $u_{2i}(t)$ with time.

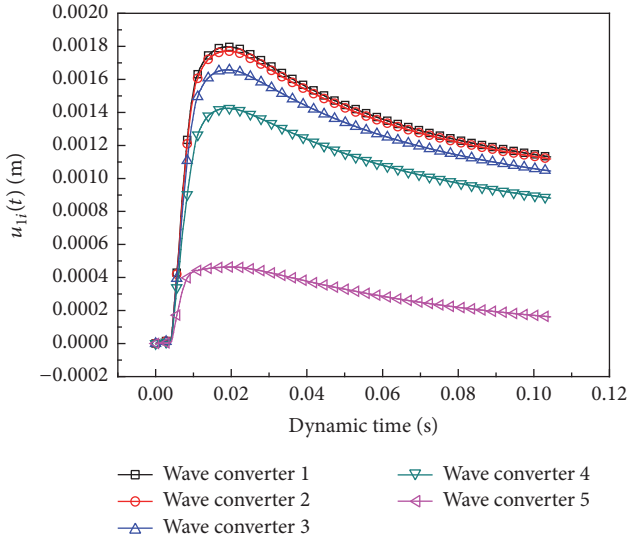


FIGURE 13: Curves of $u_{1i}(t)$ with time.

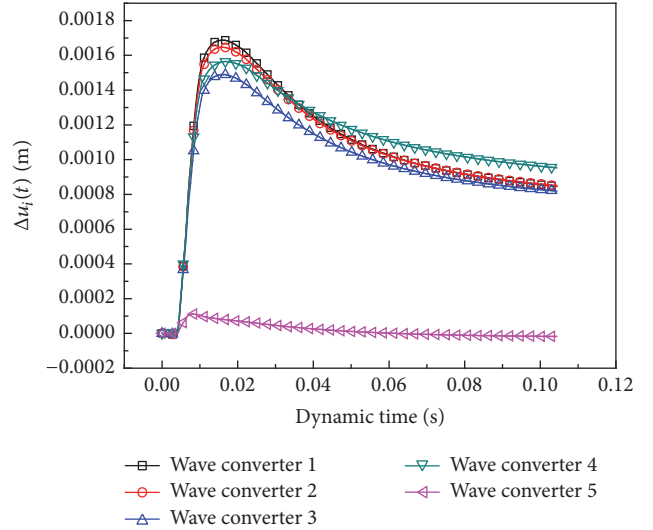


FIGURE 15: Curves of $\Delta u_i(t)$ with time.

span center. The decrease of the axial tensile stress presents that the tensile failure in the roof can be alleviated via the wave converters.

The curves of the vertical normal stresses for inner and outer elements in the span center with time are shown in Figure 18. The positive value stands for the vertical tensile stress, while the negative value stands for the vertical compressive stress. After the adoption of wave converters, the peak vertical tensile stress for inner element in the span center drops from 0.055 MPa to 0.019 MPa, which means that the possibility of spalling damage for roof is reduced. The peak vertical compressive stress for outer element in the span center drops from 1.73 MPa to 0.153 MPa, which means that the impact load acting on the roof is reduced.

The peak horizontal tensile stresses of monitoring sections for roof in 2 cases are shown in Figure 19. For case 2

with wave converters, the peak horizontal tensile stresses of inner elements for roof are generally lower than that of case 1, with a maximum decrease of 60%. Though the peak horizontal tensile stresses of outer elements for roof become higher than that of case 1, the peak horizontal tensile stresses after increasing are not very large on the whole. Via increasing the spring stiffness, the increase of the peak horizontal tensile stresses of outer elements for roof can be adjusted. In the design process of wave converters, the vibration period of the spring oscillator should not be next to the vibration period of the underground structure.

6. Conclusions

In this paper, a new blast-resistant method based on wave converters with spring oscillator for underground structures is put forward. The conception and calculation process of this

TABLE 4: Internal forces of the structure for monitoring sections 1–5.

Monitoring section	1		2		3		4		5	
Case	1	2	1	2	1	2	1	2	1	2
Bending moment (N · m)										
Minimum	733	-43847	640	-45141	365	-56001	243	-92795	-290760	-129805
Maximum	221068	163402	224395	148737	222567	95049	118881	8908	348	2039
Shear force (N)										
Minimum	-27317	-15193	2360	-3988	1194	-1956	1177	0	3474	23
Maximum	-426	1037	164052	64656	439202	138742	1041408	214362	2040240	282142
Axial force (N)										
Minimum	-41094	-83637	-42568	-81050	-57842	-81420	-104766	-83599	-348627	-91759
Maximum	1666072	921440	1596560	921280	1320330	921600	788366	932400	409633	949376

TABLE 5: Internal forces of the structure for monitoring sections 6–10.

Monitoring section	6		7		8		9		10	
Case	1	2	1	2	1	2	1	2	1	2
Bending moment (N · m)										
Minimum	-246269	-74504	-60566	-34165	-20880	-16684	-20016	-12038	-30226	-27187
Maximum	-62	59448	11794	32440	20808	19901	4810	3787	10929	8644
Shear force (N)										
Minimum	-837708	-99838	-371508	-85756	-165964	-58982	-78672	-57528	-100307	-77861
Maximum	-1537	211056	-1517	90487	-953	68296	27172	105168	51451	117882
Axial force (N)										
Minimum	-3218640	-814500	-2655720	-846588	-2229240	-891240	-1992840	-936840	-1573560	-834600
Maximum	-4890	-1196	-1170	-2138	-1175	-1223	-620	-1812	-5041	-983

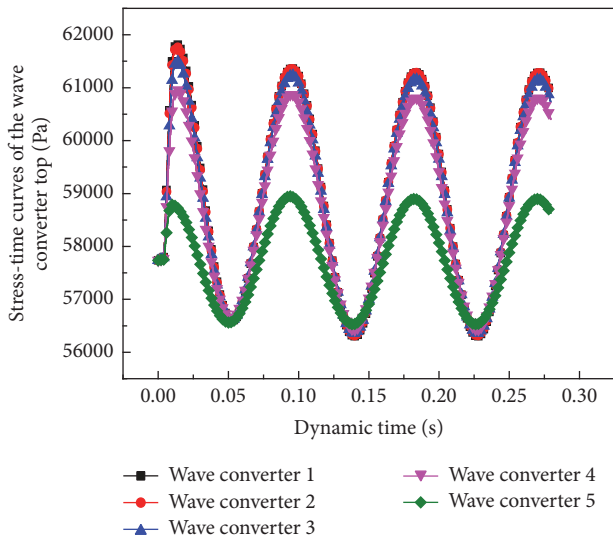


FIGURE 16: Stress-time curves of the wave converter top.

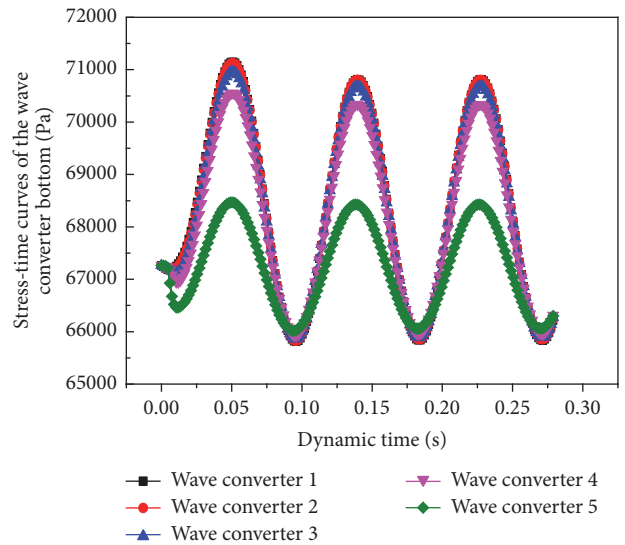


FIGURE 17: Stress-time curves of the wave converter bottom.

new method are introduced. The mechanical characteristics and motion evolution law of the wave converter are derived. The dynamic responses of the traditional underground structure and the new blast-resistant one are also calculated to verify the blast-resistant effect of the new method. The following conclusions can be drawn through the study.

- (1) After the deployment of wave converters, the peak absolute values of the bending moment, shear force, and axial force decrease generally. The decrease of the peak internal forces means that smaller size and less steel are needed in the design of the structure, which could help reduce the costs.

TABLE 6: Internal forces of the structure for monitoring sections 11–15.

Monitoring section	11		12		13		14		15	
Case	1	2	1	2	1	2	1	2	1	2
Bending moment (N · m)										
Minimum	230	664	261	614	295	555	97	419	-54210	-45028
Maximum	35258	23027	36594	23699	39747	24339	32743	15492	15725	14552
Shear force (N)										
Minimum	-421	-92	-19776	-16431	-65196	-51572	-212922	-153744	-533254	-356511
Maximum	4128	3608	319	411	-428	450	2836	718	5536	6486
Axial force (N)										
Minimum	-3124	-4749	-3185	-5153	-2953	-18050	-32879	-115840	-192165	-250929
Maximum	680160	426831	667594	419751	615300	394217	518211	354017	381111	332100

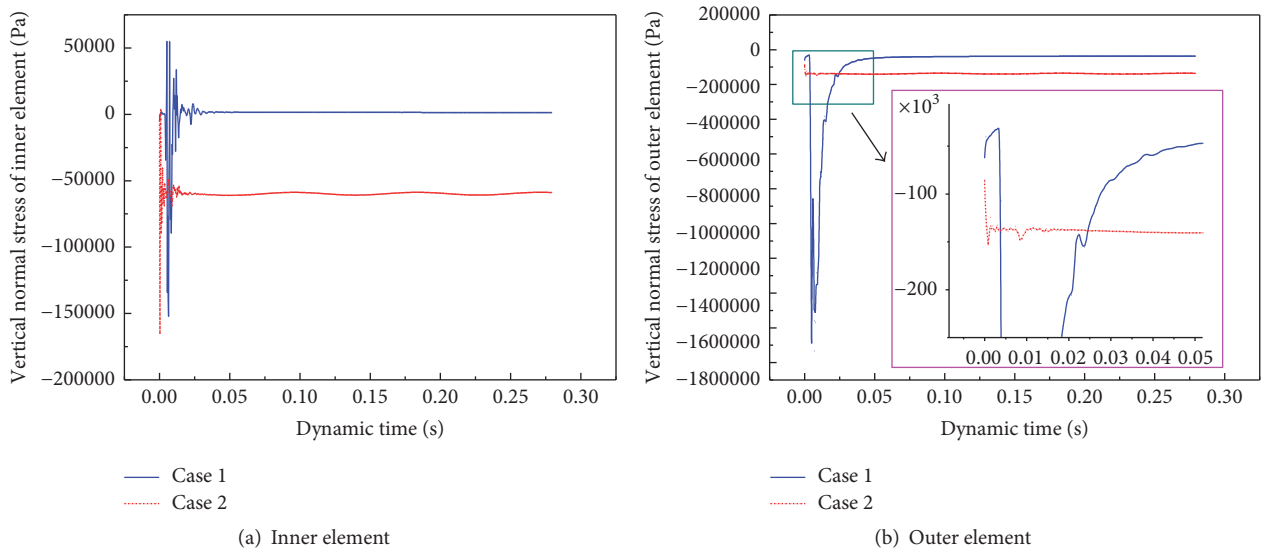


FIGURE 18: Vertical normal stress of inner and outer elements in the span center.

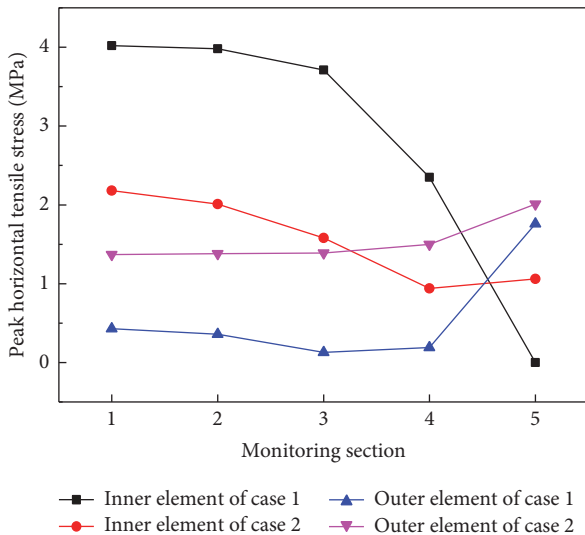


FIGURE 19: Peak horizontal tensile stress of monitoring sections for roof in 2 cases.

- (2) After the adoption of wave converters, the peak vertical tensile stress for inner element and the peak vertical compressive stress for outer element in the span center drop remarkably, which means that the possibility of spalling damage for roof is reduced, and the impact load acting on the roof is decreased.
- (3) With wave converters, the peak horizontal tensile stresses of inner elements for roof are generally lower than that of the traditional structure, which could reduce the amount of reinforcing bars.

Conflicts of Interest

The authors declare that there are no conflicts of interest regarding the publication of this paper.

Acknowledgments

The authors gratefully acknowledge the support from Chongqing Graduate Student Innovation Project under

Grant no. CYB14103, Chongqing Research Program of Basic Research and Frontier Technology under Grants nos. cstc2014jcyjA30015, cstc2015 jcyjBX0073, cstc2014jcyjA30014, and cstc2015 jcyjA30005, and Science and Technology Project of Land Resources and Real Estate Management Bureau of Chongqing Government under Grant no. CQGT-KJ-2014052.

References

- [1] V. R. Feldgun, A. V. Kochetkov, Y. S. Karinski, and D. Z. Yankelevsky, "Blast response of a lined cavity in a porous saturated soil," *International Journal of Impact Engineering*, vol. 35, no. 9, pp. 953–966, 2008.
- [2] G.-F. Gao, Y.-C. Li, K. Zhao, and Y.-C. Pang, "Dispersion and attenuation effects on stress waves in defense layer with cylindrical shell embedded," *Journal of Vibration and Shock*, vol. 30, no. 12, pp. 195–200, 2011.
- [3] Z.-L. Wang, J. G. Wang, Y.-C. Li, and C. F. Leung, "Attenuation effect of artificial cavity on air-blast waves in an intelligent defense layer," *Computers and Geotechnics*, vol. 33, no. 2, pp. 132–141, 2006.
- [4] Z. W. Liao, Q. J. Liu, and Z. M. Tian, "Tests on the explosion resistance capacity of steel plate-polyurethane foam composite sandwich plates," *Chinese Journal of Underground Space and Engineering*, vol. 1, no. 3, pp. 401–404, 2005.
- [5] S. Q. Shi, X. J. Zhang, and P. Yin, "Static analysis of the new defensive structure under explosive loading," *Underground Space*, vol. 23, no. 1, pp. 66–68, 2003.
- [6] G. S. Dhaliwal and G. M. Newaz, "Effect of layer structure on dynamic response and failure characteristics of carbon fiber reinforced aluminum laminates (CARALL)," *Journal of Dynamic Behavior of Materials*, vol. 2, no. 3, pp. 399–409, 2016.
- [7] H. C. He and D. G. Tang, "Study on flexural resistance of component strengthened by carbon fiber reinforced plastics under explosive blast," *Journal of PLA University of Science and Technology*, vol. 3, no. 6, pp. 68–73, 2002.
- [8] C. J. Montgomery, R. M. Morison, and D. O. Tutty, "Design and construction of a buried precast prestressed concrete arch," *Precast/Prestressed Concrete Institute Journal*, vol. 38, no. 1, pp. 40–57, 1993.
- [9] S. H. Yang, B. Liang, J. C. Gu, J. Shen, and A. M. Chen, "Research on characteristics of prestress change of anchorage cable in anti-explosion model test of anchored cavern," *Chinese Journal of Rock Mechanics and Engineering*, vol. 25, no. s2, pp. 3749–3756, 2006.
- [10] S. Kobiela, T. Krauthammer, and A. Walczak, "Ground shock attenuation on a buried cylindrical structure by a barrier," *Shock and Vibration*, vol. 14, no. 5, pp. 305–320, 2007.
- [11] S. Kobiela and T. Krauthammer, "Dynamic response of buried silo caused by underground explosion," *Shock and Vibration*, vol. 11, no. 5-6, pp. 665–684, 2004.
- [12] V. Yakushin, L. Bel'kova, and I. Sevastyanova, "Properties of rigid polyurethane foams filled with glass microspheres," *Mechanics of Composite Materials*, vol. 48, no. 5, pp. 579–586, 2012.
- [13] A. M. Alhozaimy, P. Soroushian, and F. Mirza, "Mechanical properties of polypropylene fiber reinforced concrete and the effects of pozzolanic materials," *Cement and Concrete Composites*, vol. 18, no. 2, pp. 85–92, 1996.
- [14] A. R. Khaloo, M. Dehestani, and P. Rahmatabadi, "Mechanical properties of concrete containing a high volume of tire-rubber particles," *Waste Management*, vol. 28, no. 12, pp. 2472–2482, 2008.
- [15] F. Hernández-Olivares and G. Barluenga, "Fire performance of recycled rubber-filled high-strength concrete," *Cement and Concrete Research*, vol. 34, no. 1, pp. 109–117, 2004.
- [16] S. K. Lim, C. S. Tan, O. Y. Lim, and Y. L. Lee, "Fresh and hardened properties of lightweight foamed concrete with palm oil fuel ash as filler," *Construction and Building Materials*, vol. 46, no. 3, pp. 39–47, 2013.
- [17] R. Cortell, "Application of the fourth-order Runge-Kutta method for the solution of high-order general initial value problems," *Computers & Structures*, vol. 49, no. 5, pp. 897–900, 1993.
- [18] B. S. Desale and N. R. Dasre, "Numerical solution of the system of six coupled nonlinear ODEs by Runge-Kutta fourth order method," *Applied Mathematical Sciences*, vol. 7, no. 6, pp. 287–305, 2013.
- [19] J. B. Liu, Y. X. Du, and Q. S. Yan, "Dynamic response of underground box structures subjected to blast load," *Journal of PLA University of Science and Technology*, vol. 8, no. 5, pp. 520–524, 2007.
- [20] B. Zhang, J. Y. Xu, L. Li, and W. Lin, "Analysis of antidetontational property of foam concrete backfill layers in underground compound structure," *Sichuan Building Science*, vol. 36, no. 6, pp. 135–138, 2010.
- [21] X. P. Li, J. H. Chen, Y. H. Li, and Y. F. Dai, "Study of blasting seismic effects of underground chamber group in Xiluodu hydropower station," *Chinese Journal of Rock Mechanics and Engineering*, vol. 29, no. 3, pp. 493–501, 2010.



Hindawi

Submit your manuscripts at
<https://www.hindawi.com>

